Computer Modeling in Engineering & Sciences

Tech Science Press

https://doi.org/10.32604/cmes.2026.078247

ARTICLE

Machine Learning-Based Power Allocation for Covert Communication in LEO Satellite–UAV Cooperative Networks

Minjeong Kang[1], **Jung Hoon Lee**[1,*] **and Il-Gu Lee**[2,*]

[1]Department of Electronics Engineering and Applied Communications Research Center, Hankuk University of Foreign Studies, Yongin, Republic of Korea

[2]Department of Future Convergence Technology Engineering, Sungshin Women's University, Seoul, Republic of Korea

*Corresponding Authors: Jung Hoon Lee. Email: tantheta@hufs.ac.kr; Il-Gu Lee. Email: iglee@sungshin.ac.kr

Received: 27 December 2025; Accepted: 02 March 2026; Published: 27 April 2026

ABSTRACT: In next-generation non-terrestrial network environments, the increasing risk of detection by unauthorized observers has motivated extensive research on covert communication approaches that minimize the probability of detection. In particular, jamming-assisted cooperative covert communication has attracted significant attention as an effective approach to simultaneously ensure communication performance and security, leading to growing interest in cooperative architectures among heterogeneous platforms. This study investigates covert communication in Low Earth Orbit (LEO) satellite–unmanned aerial vehicle (UAV) cooperative networks, where the LEO satellite serves a legitimate user, while the UAV acts as a cooperative jammer to enhance covertness. A network that integrates a LEO satellite with wide service coverage and a UAV with high mobility offers flexible support for covert communication in diverse environments. However, the problem of optimally allocating power between the LEO satellite and UAV while satisfying the covert communication constraint inherently exhibits a non-convex structure, which commonly necessitates a discretized grid-search baseline over feasible candidate combinations. As the number of candidates increases, this approach suffers from rapidly increasing computational complexity. To address this computational burden, this study proposes a machine-learning (ML)–based power-allocation scheme. The proposed ML model leverages key channel-related and covertness-related features to efficiently select an effective pair of power scaling factors, while significantly reduced computational complexity. Simulation results demonstrate that the proposed scheme achieves comparable average covert rate to that of the discretized grid-search baseline while requiring substantially lower computational complexity. These results further indicate that the proposed scheme enables low-latency and efficient power control in LEO satellite–UAV cooperative networks. Finally, future work will extend the proposed scheme to more complex multi-LEO satellite–UAV cooperative scenarios through joint optimization of additional system parameters.

KEYWORDS: Low earth orbit (LEO) satellite communications; unmanned aerial vehicle (UAV) cooperative jamming; covert communication; power allocation; machine learning (ML)

1 Introduction

Security in wireless communication systems has been widely regarded as a fundamental research topic for protecting confidential information from unauthorized receivers. Accordingly, a wide range of security techniques based on physical-layer security (PLS) and encryption have been extensively investigated. However, most PLS schemes rely heavily on channel state information (CSI), and their security performance can be significantly degraded if adversaries obtain access to this information. Encryption-based approaches

inherently suffer from a risk of secret key leakage, which cannot be entirely eliminated. These limitations highlight the need for a robust security paradigm that complements conventional security mechanisms.

Motivated by these limitations, covert communication, aiming to conceal the transmitted information, as well as the existence of wireless transmissions from unauthorized wardens, has emerged as a new paradigm for secure communication. Covert communication aims to reduce the reliability of a warden's detection by increasing both false-alarm and miss-detection probabilities when determining the presence of a transmission [1]. These covert communication techniques have been extensively investigated in terrestrial wireless network environments. In particular, the authors in [2] showed that, in quasi-static fading environments with channel uncertainty, the detection performance of a warden becomes largely insensitive to the accuracy of CSI when the detection error probability is sufficiently high. Meanwhile, the authors in [3] proposed a scheme that employs full-duplex decode-and-forward user relaying to achieve perfect cancellation of covert signals at the warden. Moreover, the authors in [4] analyzed the covert transmission rate of a wireless relay system by optimizing the transmit power while jointly considering cooperative jamming and relay selection. In addition, the authors in [5] investigated covert communication in more complex scenarios, where the fundamental trade-off between covertness requirements and secrecy transmission rate was analyzed in the presence of untrusted relay nodes and multiple wardens through jamming-based power allocation. Similarly, the authors in [6] considered covert communication in multi-antenna amplify-and-forward relaying networks, where the relay was designed to simultaneously forward confidential signals and transmit artificial noise, and relay precoding and power allocation were optimized based on CSI to enhance covertness performance. Furthermore, covert communication schemes that leverage intelligent aerial platforms have been proposed. Specifically, the authors in [7] presented a covert communication framework that integrated an unmanned aerial vehicle (UAV) with an intelligent reflecting surface (IRS), where the transmit power, IRS phase shifts, and UAV location were jointly optimized to maximize the covert transmission rate under the worst-case detection conditions. Similarly, the authors in [8] proposed a covert communication framework for reconfigurable intelligent surface (RIS)-assisted cooperative networks, where power allocation was optimized to simultaneously enhance covertness and PLS by reducing both the detection error probability and the eavesdropping probability.

With the expansion of wireless network coverage across terrestrial, aerial, and space domains, research on covert communication has extended beyond terrestrial and aerial networks to space–air integrated networks. Among these architectures, systems that integrate Low Earth Orbit (LEO) satellites with UAVs have attracted significant attention owing to their ability to provide wide service coverage and high operational flexibility [9]. In this context, the authors in [10] analyzed covert communication performance in space–air–ground integrated networks by accounting for practical impairments such as channel estimation errors, hardware imperfections, and co-channel interference, and highlighted the importance of power allocation and CSI accuracy. In addition, the authors in [11] studied covert communication in a space–air–ground integrated network with a dual-hop transmission structure, where finite block-length communication was considered and the covert outage probability was analyzed under artificial noise (AN)-assisted jamming, thereby revealing the impact of key system parameters on covertness performance. The authors in [12] proposed a game-theoretic approach for covert communication in large-scale multi-tier LEO satellite networks, where UAVs are considered service nodes supported by a satellite backhaul, thereby simultaneously improving transmission reliability and coverage while maintaining terrestrial wardens. Meanwhile, the authors in [13] investigated a covert communication system employing UAVs as relays from a practical system design perspective and proposed a scheme to optimize the effective covert transmission rate in Rician fading environments by leveraging full-duplex cooperative jamming. In a related line of work, the authors in [14] analytically investigated the uplink outage probability in full-duplex multiple-input multiple-output

(MIMO)-based cooperative communications between autonomous aerial vehicles and intelligent connected vehicles by accounting for interference, and proposed low-complexity approximation methods. In addition, the authors of [15] studied channel prediction for UAV–LEO satellite links and proposed a lightweight channel prediction network based on multilayer perceptrons, which improves prediction accuracy while reducing computational complexity.

Machine learning (ML) has emerged as an effective tool for reducing the high computational complexity associated with resource allocation and signal processing problems in wireless and satellite networks. In [16], the authors employed a deep neural network (DNN) to predict the optimal decoding order for successive interference cancellation in multiuser multiple-input single-output (MISO) non-orthogonal multiple access systems, which significantly reduced the computational complexity of an exhaustive search while achieving near-optimal performance. In addition, the authors in [17] introduced a model-free actor–critic reinforcement learning–based resource allocation framework for satellite networks supporting the Internet of Remote Things, which jointly optimizes power allocation and data scheduling in dynamic channels and energy harvesting environments. Along similar lines, the authors in [18] proposed a resource allocation scheme for the non-terrestrial network uplink that combines long short-term memory–based channel prediction with deep reinforcement learning to cope with time-varying channels, thereby maximizing the uplink transmission rate while ensuring fairness and minimizing latency. In addition, the authors in [19] developed a deep Q-network–based scheduling algorithm for beam-hopping LEO satellite communication systems, which jointly optimizes time-slot allocation and power control to satisfy traffic demands while minimizing the total power consumption. Moreover, to address frequent handover issues in LEO satellite networks, the authors in [20] proposed a distributed multi-agent deep reinforcement learning-based handover strategy. Furthermore, Ref. [21] proposed a hybrid framework that combined convex optimization with deep learning for LEO satellite downlink networks, enabling efficient solutions to NP-hard joint channels and power allocation problems. Moreover, the authors in [22] presented a joint design for channel estimation, multiuser detection, and resource allocation based on deep learning for satellite NOMA systems, which significantly improved the bit error rate performance in time-varying channel environments. Finally, the authors in [23] proposed a joint optimization framework based on deep reinforcement learning for UAV–RIS–assisted Internet of Vehicles networks, aiming to maximize secrecy energy efficiency.

Motivated by these studies, this study proposes an ML-based power allocation scheme for covert communication in LEO satellite–UAV cooperative networks. The proposed scheme leverages the wide coverage of LEO satellites and the mobility of UAVs to enhance covert communication performance, while employing an ML model to significantly reduce the computational complexity associated with power allocation. In the considered framework, the UAV acts as a cooperative jammer by transmitting AN, while the learning model adopts a DNN architecture to predict an effective pair of power scaling factors. Simulation results demonstrate that the proposed scheme achieves a performance comparable average covert rate to that of a discretized grid-search baseline, with substantially lower computational complexity.

The remainder of this paper is organized as follows. Section 3 describes the system model and formulates the covert communication problem. Section 4 presents the proposed ML-based power allocation scheme. Section 5 evaluates the performance through numerical simulations, and Section 6 concludes the paper.

2 Notation

Table 1 lists the main mathematical symbols used in this paper.

Table 1: List of notations.

Notation	Description
N_U	Number of antenna elements at Alice
N_x, N_y	Number of antenna elements along the x- and y-axes
$\mathbf{h}_{AB}, \mathbf{h}_{AW}$	Channels from Alice to Bob/Willie
$\mathbf{h}_{CB}, \mathbf{h}_{CW}$	Channels from Charlie to Bob/Willie
$K_{AB}, K_{AW}, K_{CB}, K_{CW}$	Rician K-factors of the corresponding channels
$\mathbf{a}_A(\phi, \theta)$	Steering vector at Alice
$\mathbf{a}_C(\phi)$	Steering vector at Charlie
ϕ, θ	Azimuth and elevation angles
P_A, P_C	Maximum transmit powers
α_A, α_C	Power scaling factors
$\mathbf{w}_A, \mathbf{w}_C$	Beamforming vectors
SINR_B	Signal-to-interference-plus-noise ratio at Bob
R_c	Achievable covert rate
B	Number of observation samples at Willie
τ	Detection threshold
$P_{\mathrm{FA}}, P_{\mathrm{MD}}$	False alarm and misdetection probabilities
ξ	Total detection error probability
ϵ	Allowable detection error probability
γ	Discretization step size of effective power scaling factors
$\mathcal{Q}$	Discretized set of effective power scaling factors

3 System Model

The considered system model is illustrated in Fig. 1. Specifically, we considered an LEO satellite–UAV cooperative network for covert communications comprising an LEO satellite (Alice) equipped with an N_U-element uniform planar array (UPA), a UAV (Charlie) equipped with a two-element uniform linear array (ULA) that acts as a cooperative jammer, a legitimate user (Bob), and a warden (Willie), each equipped with a single antenna.

The UPA at Alice consists of $N_U = N_x \times N_y$ antenna elements, where N_x and N_y represent the number of antennas along the x- and y-axes, respectively. The channel vector from Alice to Bob is denoted by $\mathbf{h}_{AB} \in \mathbb{C}^{N_U \times 1}$, and $\mathbf{h}_{AW} \in \mathbb{C}^{N_U \times 1}$ represents the channel from Alice to Willie. Moreover, $\mathbf{h}_{CB} \in \mathbb{C}^{2\times 1}$ and $\mathbf{h}_{CW} \in \mathbb{C}^{2\times 1}$ denote the channels from Charlie to Bob and from Charlie to Willie, respectively. All the channels were modeled as Rician fading channels. We assume that perfect CSI of all relevant channels is available at the UAV for power scaling factor selection.

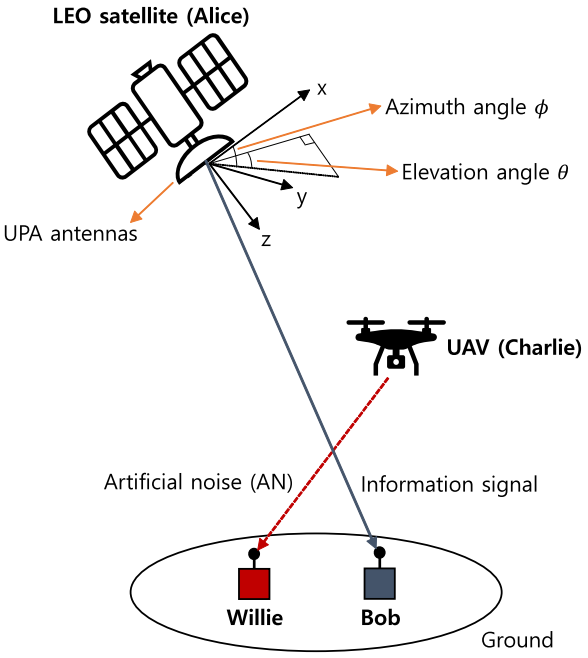

Figure 1: System model of the considered LEO satellite–UAV cooperative covert communication network.

The channels from Alice to Bob and Alice to Willie are as follows:

$$\mathbf{h}_{AB} = \sqrt{\frac{K_{AB}}{K_{AB}+1}}\,\mathbf{h}_{AB}^{\mathrm{LoS}} + \sqrt{\frac{1}{K_{AB}+1}}\,\mathbf{h}_{AB}^{\mathrm{NLoS}},$$
$$\mathbf{h}_{AW} = \sqrt{\frac{K_{AW}}{K_{AW}+1}}\,\mathbf{h}_{AW}^{\mathrm{LoS}} + \sqrt{\frac{1}{K_{AW}+1}}\,\mathbf{h}_{AW}^{\mathrm{NLoS}}. \tag{1}$$

The Alice-Bob and Alice-Willie channels are characterized by the Rician K-factors K_{AB} and K_{AW} that determine the contributions of the deterministic line-of-sight (LoS) components $\mathbf{h}_{AB}^{\mathrm{LoS}}$ and $\mathbf{h}_{AW}^{\mathrm{LoS}}$. The corresponding non-line-of-sight (NLoS) components are denoted by $\mathbf{h}_{AB}^{\mathrm{NLoS}}$ and $\mathbf{h}_{AW}^{\mathrm{NLoS}}$, respectively. The NLoS components are modeled as the superposition of multiple scattered paths.

The LoS components of Alice are defined as follows:

$$\mathbf{h}_{AB}^{\mathrm{LoS}} = m_{AB}\exp\Big(j2\pi\big(f_{AB}^{\mathcal{D},\mathrm{LoS}} - f_c\tau_{AB}^{\mathrm{LoS}}\big)\Big)\,\mathbf{a}_A(\phi_{AB},\theta_{AB}),$$
$$\mathbf{h}_{AW}^{\mathrm{LoS}} = m_{AW}\exp\Big(j2\pi\big(f_{AW}^{\mathcal{D},\mathrm{LoS}} - f_c\tau_{AW}^{\mathrm{LoS}}\big)\Big)\,\mathbf{a}_A(\phi_{AW},\theta_{AW}). \tag{2}$$

Under the above assumptions, the NLoS components of Alice are expressed as:

$$\mathbf{h}_{AB}^{\mathrm{NLoS}} = \frac{1}{\sqrt{L_{AB}}}\sum_{l=1}^{L_{AB}} m_{AB,l}\exp\Big(j2\pi\big(f_{AB,l}^{\mathcal{D},\mathrm{NLoS}} - f_c\tau_{AB,l}^{\mathrm{NLoS}}\big)\Big)\,\mathbf{a}_A(\phi_{AB,l},\theta_{AB,l}),$$
$$\mathbf{h}_{AW}^{\mathrm{NLoS}} = \frac{1}{\sqrt{L_{AW}}}\sum_{l=1}^{L_{AW}} m_{AW,l}\exp\Big(j2\pi\big(f_{AW,l}^{\mathcal{D},\mathrm{NLoS}} - f_c\tau_{AW,l}^{\mathrm{NLoS}}\big)\Big)\,\mathbf{a}_A(\phi_{AW,l},\theta_{AW,l}). \tag{3}$$

Here, $\mathbf{a}_A(\phi,\theta)$ denotes the array steering vector at Alice, where ϕ and θ represent the azimuth and elevation angles, respectively. Moreover, m_{AB} and m_{AW} denote the complex-valued channel gains of the LoS

components, while $m_{AB,l}$ and $m_{AW,l}$ represent the complex-valued channel gains of the lth NLoS paths. f_c denotes the carrier frequency, and $f_{AB}^{\mathcal{D},\mathrm{LoS}}$ and $f_{AW}^{\mathcal{D},\mathrm{LoS}}$ denote the Doppler shifts associated with the LoS paths, whereas $f_{AB}^{\mathcal{D},\mathrm{NLoS}}$ and $f_{AW}^{\mathcal{D},\mathrm{NLoS}}$ represent the Doppler shifts corresponding to the NLoS paths. Similarly, τ_{AB}^{LoS} and τ_{AW}^{LoS} denote the propagation delays of the LoS components, while $\tau_{AB,l}^{\mathrm{NLoS}}$ and $\tau_{AW,l}^{\mathrm{NLoS}}$ denote the propagation delays of the lth NLoS components. Finally, L_{AB} and L_{AW} in (3) represent the number of NLoS paths for the Alice-Bob and Alice-Willie channels, respectively.

The UPA steering vector is defined as:

$$\mathbf{a}_A(\phi,\theta) = \mathbf{a}_A^x(\phi,\theta) \otimes \mathbf{a}_A^y(\phi,\theta), \tag{4}$$

where $\otimes$ denotes the Kronecker product. Vectors $\mathbf{a}_A^x(\phi,\theta)$ and $\mathbf{a}_A^y(\phi,\theta)$ are defined as follows:

$$\begin{aligned}
\mathbf{a}_A^x(\phi,\theta) &= \frac{1}{\sqrt{N_x}}\left[1, e^{j\frac{2\pi}{\lambda}d\sin\theta\cos\phi}, \ldots, e^{j\frac{2\pi}{\lambda}d(N_x-1)\sin\theta\cos\phi}\right]^T, \\
\mathbf{a}_A^y(\phi,\theta) &= \frac{1}{\sqrt{N_y}}\left[1, e^{j\frac{2\pi}{\lambda}d\sin\theta\sin\phi}, \ldots, e^{j\frac{2\pi}{\lambda}d(N_y-1)\sin\theta\sin\phi}\right]^T,
\end{aligned} \tag{5}$$

where the inter-element spacing is set to $d = \lambda/2$. The UPA steering vector is normalized to the unit norm.

Furthermore, the channels from Charlie to Bob and Charlie to Willie are denoted by:

$$\begin{aligned}
\mathbf{h}_{CB} &= \sqrt{\frac{K_{CB}}{K_{CB}+1}}\,\mathbf{h}_{CB}^{\mathrm{LoS}} + \sqrt{\frac{1}{K_{CB}+1}}\,\mathbf{h}_{CB}^{\mathrm{NLoS}}, \\
\mathbf{h}_{CW} &= \sqrt{\frac{K_{CW}}{K_{CW}+1}}\,\mathbf{h}_{CW}^{\mathrm{LoS}} + \sqrt{\frac{1}{K_{CW}+1}}\,\mathbf{h}_{CW}^{\mathrm{NLoS}}.
\end{aligned} \tag{6}$$

The channels associated with Charlie follow a structure similar to those of Alice, where K_{CB} and K_{CW} represent the Rician K-factors of the Charlie-Bob and Charlie-Willie channels, respectively.

The LoS components of Charlie are defined as follows:

$$\begin{aligned}
\mathbf{h}_{CB}^{\mathrm{LoS}} &= m_{CB}\exp\left(j2\pi\left(f_{CB}^{\mathcal{D},\mathrm{LoS}} - f_c\tau_{CB}^{\mathrm{LoS}}\right)\right)\mathbf{a}_C(\phi_{CB}), \\
\mathbf{h}_{CW}^{\mathrm{LoS}} &= m_{CW}\exp\left(j2\pi\left(f_{CW}^{\mathcal{D},\mathrm{LoS}} - f_c\tau_{CW}^{\mathrm{LoS}}\right)\right)\mathbf{a}_C(\phi_{CW}).
\end{aligned} \tag{7}$$

Similarly, the NLoS components associated with Charlie are given by:

$$\begin{aligned}
\mathbf{h}_{CB}^{\mathrm{NLoS}} &= \frac{1}{\sqrt{L_{CB}}}\sum_{l=1}^{L_{CB}} m_{CB,l}\exp\left(j2\pi\left(f_{CB,l}^{\mathcal{D},\mathrm{NLoS}} - f_c\tau_{CB,l}^{\mathrm{NLoS}}\right)\right)\mathbf{a}_C(\phi_{CB,l}), \\
\mathbf{h}_{CW}^{\mathrm{NLoS}} &= \frac{1}{\sqrt{L_{CW}}}\sum_{l=1}^{L_{CW}} m_{CW,l}\exp\left(j2\pi\left(f_{CW,l}^{\mathcal{D},\mathrm{NLoS}} - f_c\tau_{CW,l}^{\mathrm{NLoS}}\right)\right)\mathbf{a}_C(\phi_{CW,l}).
\end{aligned} \tag{8}$$

Here, $\mathbf{a}_C(\phi)$ denotes the array steering vector at Charlie. Since Charlie employs a two-element ULA, only the azimuth angle is considered.

$$\mathbf{a}_C(\phi) = \frac{1}{\sqrt{2}}\left[1, e^{j\frac{2\pi}{\lambda}d\sin\phi}\right]^T. \tag{9}$$

The array steering vector is normalized to the unit norm.

The transmitted signals of Alice and Charlie can be expressed as:

$$\mathbf{x}_A = \mathbf{w}_A\sqrt{\alpha_A P_A}s,$$
$$\mathbf{x}_C = \mathbf{w}_C\sqrt{\alpha_C P_C}z, \quad z \sim \mathcal{CN}(0,1), \tag{10}$$

where $\mathbf{w}_A \in \mathbb{C}^{N_U \times 1}$ and $\mathbf{w}_C \in \mathbb{C}^{2\times 1}$ represent the beamforming vectors used by Alice and Charlie, respectively. Alice and Charlie do not share their transmit power budgets, and each node is subject to its own total transmit power constraint. Thus, the beamforming vectors were normalized as $\|\mathbf{w}_A\| = 1$ and $\|\mathbf{w}_C\| = 1$. Here, P_A and P_C denote the maximum transmit powers of Alice and Charlie, respectively. For simplicity, we consider $P_A = P_C$. The parameters $\alpha_A \in [0,1]$ and $\alpha_C \in [0,1]$ are the power scaling factors. For Alice, s denotes the information signal intended for Bob. Charlie transmits AN to Willie, where $z \sim \mathcal{CN}(0,1)$ denotes the corresponding AN symbol modeled as a circularly symmetric complex Gaussian random variable with zero mean and unit variance.

Thus, the signals received by Bob and Willie are denoted by:

$$y_B = \mathbf{h}_{AB}^{\dagger}\mathbf{x}_A + \mathbf{h}_{CB}^{\dagger}\mathbf{x}_C + n_B,$$
$$y_W = \mathbf{h}_{AW}^{\dagger}\mathbf{x}_A + \mathbf{h}_{CW}^{\dagger}\mathbf{x}_C + n_W, \tag{11}$$

where n_B and n_W represent the circularly symmetric complex Gaussian noise at Bob and Willie, respectively, with zero mean and unit variance, that is, $n_B, n_W \sim \mathcal{CN}(0,1)$. Therefore, the signal-to-interference-plus-noise ratio (SINR) at Bob's end is expressed as:

$$\mathsf{SINR}_B = \frac{\alpha_A P_A |\mathbf{h}_{AB}^{\dagger}\mathbf{w}_A|^2}{\alpha_C P_C |\mathbf{h}_{CB}^{\dagger}\mathbf{w}_C|^2 + 1}. \tag{12}$$

Alice employs maximum ratio transmission (MRT) beamforming to maximize the received signal power at Bob. Accordingly, the MRT beamforming vector at Alice is given by:

$$\mathbf{w}_A = \frac{\mathbf{h}_{AB}}{\|\mathbf{h}_{AB}\|}. \tag{13}$$

In contrast, Charlie adopts zero-forcing (ZF) beamforming for AN transmission, which is designed to lie in the null space of the Charlie–Bob channel in order to avoid causing interference to Bob. Since Charlie is equipped with a two-element ULA and Bob employs a single antenna, the null space of the Charlie–Bob channel is one-dimensional, which guarantees the existence of a non-trivial ZF beamforming vector. Specifically, Charlie's ZF beamforming vector $\mathbf{w}_C$ is constructed as:

$$\mathbf{w}_C = \frac{\left(\mathbf{I} - \frac{\mathbf{h}_{CB}\mathbf{h}_{CB}^{\dagger}}{\|\mathbf{h}_{CB}\|^2}\right)\mathbf{h}_{CW}}{\left\|\left(\mathbf{I} - \frac{\mathbf{h}_{CB}\mathbf{h}_{CB}^{\dagger}}{\|\mathbf{h}_{CB}\|^2}\right)\mathbf{h}_{CW}\right\|}. \tag{14}$$

Consequently, the ZF beamforming vector satisfies the following null-space constraint:

$$\mathbf{h}_{CB}^{\dagger}\mathbf{w}_C = 0. \tag{15}$$

This ensures that the AN transmitted by Charlie is completely nulled at Bob's receiver. Consequently, the interference term in (12) vanishes, and the SINR at Bob simplifies to:

$$\mathsf{SINR}_B = \alpha_A P_A |\mathbf{h}_{AB}^{\dagger} \mathbf{w}_A|^2. \tag{16}$$

Thus, the achievable covert rate at Bob's end under the covert communication constraint is expressed as:

$$\mathsf{R}_c = \log_2(1 + \mathsf{SINR}_B). \tag{17}$$

Willie used an energy detector and performs a binary hypothesis test over B observation samples (channel uses) to detect Alice's transmissions. Accordingly, the detection problem is formulated as:

$$\begin{cases} \mathcal{H}_0 : & y_W = \mathbf{h}_{CW}^{\dagger} \mathbf{x}_C + n_W, \quad \text{(Alice is silent)}, \\ \mathcal{H}_1 : & y_W = \mathbf{h}_{AW}^{\dagger} \mathbf{x}_A + \mathbf{h}_{CW}^{\dagger} \mathbf{x}_C + n_W, \quad \text{(Alice is active)}. \end{cases} \tag{18}$$

From (18), under $\mathcal{H}_0$, Willie observes only Charlie's AN and the background noise, whereas under $\mathcal{H}_1$, Willie observes Alice's information-bearing signal.

Specifically, Willie's test statistic is denoted by:

$$T_W = \frac{1}{B} \sum_{b=1}^{B} |y_W[b]|^2, \tag{19}$$

which measures the average energy of the received signal over B observation samples (channel uses). Accordingly, the average received power at Willie under the two hypotheses can be expressed as:

$$\begin{cases} \mathcal{H}_0 : \mu_0 & = 1 + \alpha_C P_C |\mathbf{h}_{CW}^{\dagger} \mathbf{w}_C|^2, \\ \mathcal{H}_1 : \mu_1 & = \mu_0 + \alpha_A P_A |\mathbf{h}_{AW}^{\dagger} \mathbf{w}_A|^2. \end{cases} \tag{20}$$

By invoking the central limit theorem, when B is sufficiently large, the test statistic T_W at Willie can be approximated as a Gaussian random variable under both hypotheses.

Hence, the false alarm probability (i.e., Willie deciding $\mathcal{H}_1$ when Alice is silent) is denoted by P_{FA}, and the misdetection probability (i.e., Willie deciding $\mathcal{H}_0$ when Alice is active) is denoted by P_{MD}. Therefore, the false alarm probability and misdetection probability at Willie is expressed as:

$$\begin{aligned} P_{FA} &= \Pr(T_W > \tau \mid \mathcal{H}_0), \\ P_{MD} &= \Pr(T_W \leq \tau \mid \mathcal{H}_1), \end{aligned} \tag{21}$$

where τ is the detection threshold. Thus, the total detection error probability in Willie's law is defined as:

$$\xi = P_{FA} + P_{MD}. \tag{22}$$

Willie is assumed to adopt an optimal detection threshold that minimizes ξ, representing the worst-case detection strategy in covert communication. Under this assumption, a covert communication constraint was imposed as:

$$\xi \geq 1 - \epsilon, \tag{23}$$

where $\epsilon \in (0, 1)$ is the allowable detection error probability.

To transform the probabilistic covertness constraint in (23) as an equivalent covertness constraint expressed in terms of transmit power, Pinsker's inequality is employed to lower bound the detection error probability in terms of the Kullback–Leibler (KL) divergence between the distributions under the two hypotheses [6]. Specifically, the optimal detection error probability satisfies

$$\xi \geq 1 - \sqrt{\frac{1}{2} D(\mathbb{P}_0 \| \mathbb{P}_1)}. \tag{24}$$

Accordingly, a sufficient condition to guarantee $\xi \geq 1 - \epsilon$ is given by

$$D(\mathbb{P}_0 \| \mathbb{P}_1) \leq 2\,\epsilon^2\,. \tag{25}$$

Moreover, due to the Gaussianity and mutual independence of the transmitted signals and noise components, Willie's received signal $y_W[b]$ follows a conditionally circularly symmetric complex Gaussian distribution at each observation. Under the common Doppler assumption, where the Doppler effect introduces only phase variations across observations, the average received power (variance) remains invariant over the observation interval. With independent signal and noise realizations across observations, $y_W[b]$ can be modeled as independent and identically distributed complex Gaussian random variable with variances μ_0 and μ_1 under hypotheses $\mathcal{H}_0$ and $\mathcal{H}_1$, respectively. Accordingly, the KL divergence over B observations can be expressed as

$$D(\mathbb{P}_0 \| \mathbb{P}_1) = B \left(\ln \frac{\mu_1}{\mu_0} + \frac{\mu_0}{\mu_1} - 1 \right). \tag{26}$$

In the covert communication regime, the impact of Alice's transmission on Willie's observation is sufficiently small, such that $\mu_1 \approx \mu_0$. Applying a second-order Taylor expansion yields the following approximation:

$$D(\mathbb{P}_0 \| \mathbb{P}_1) \approx \frac{B}{2} \left(\frac{\mu_1 - \mu_0}{\mu_0} \right)^2. \tag{27}$$

Substituting (27) into (25), we obtain

$$(\mu_1 - \mu_0)^2 \leq \frac{4\,\epsilon^2}{B} \mu_0^2. \tag{28}$$

Finally, by substituting (20) into (28), Alice's transmit power is constrained to satisfy the following condition:

$$\left(\alpha_A P_A \left| \mathbf{h}_{AW}^{\dagger} \mathbf{w}_A \right|^2 \right)^2 \leq \frac{4\,\epsilon^2}{B} \left(1 + \alpha_C P_C \left| \mathbf{h}_{CW}^{\dagger} \mathbf{w}_C \right|^2 \right)^2. \tag{29}$$

However, obtaining power scaling factors α_A and α_C that maximize the covert rate is not straightforward. This is because the covert communication constraint is nonlinear and the power scaling factors assume continuous values, making the resulting optimization problem computationally prohibitive. To address this issue, this study approximates the power scaling factors using a discretized set with step size γ, where $0 < \gamma \leq 1$, thereby transforming the original continuous optimization problem into one with a finite search space. Therefore, the discretized set of effective power scaling factors is defined as:

$$\mathcal{Q} = \{0, \gamma, 2\gamma, \ldots, 1\}. \tag{30}$$

Based on the discretized set $\mathcal{Q}$, the number of candidate effective power scaling factor combinations was $|\mathcal{Q}|^2 = ((1/\gamma)+1)^2$. Accordingly, the effective power scaling factor combination that maximizes the covert rate can be obtained by solving the following optimization problem:

$$\begin{aligned} \underset{\alpha_A,\alpha_C\in\mathcal{Q}}{\text{maximize}} \quad & \mathsf{R}_c(\alpha_A) \\ \text{s.t.} \quad & \left(\alpha_A P_A \left|\mathbf{h}_{AW}^{\dagger}\mathbf{w}_A\right|^2\right)^2 \le \frac{4\,\epsilon^2}{B}\left(1+\alpha_C P_C \left|\mathbf{h}_{CW}^{\dagger}\mathbf{w}_C\right|^2\right)^2, \\ & 0 \le \alpha_A, \alpha_C \le 1. \end{aligned} \tag{31}$$

Under the above formulation, the covert rate is computed for all effective power scaling factor combinations. Specifically, when the covert constraint (29) is satisfied, the covert rate is evaluated in the usual manner, whereas it is defined as zero otherwise. This definition can be explicitly expressed as:

$$\mathsf{R}_c(\alpha_A) = \begin{cases} \log_2\left(1+\mathsf{SINR}_B\right), & \text{if the covert constraint (29) is satisfied,} \\ 0, & \text{otherwise.} \end{cases} \tag{32}$$

As the optimization of the effective power scaling factor combination is performed over a discretized set rather than a continuous domain via a grid search, the solution obtained from (31) is regarded as discretized grid-search baseline. Under ZF beamforming, α_C does not affect the achievable covert rate at Bob's end and is therefore introduced only through the covert constraint (29). As the discretization step size γ decreased, the performance gap with respect to the optimal solution of the corresponding continuous optimization problem was reduced. However, the number of candidate power allocation coefficient combinations increases in the order $\mathcal{O}(|\mathcal{Q}|^2)$, causing a rapid increase in computational complexity. To alleviate this computational burden, this study employed ML techniques to efficiently identify an effective power scaling factor combination from a candidate set with reduced computational complexity.

4 ML-Based Power Allocation Scheme

In this section, we describe the proposed power allocation scheme in detail. First, we explain the role of the ML model in the proposed scheme and then provide a detailed description of its architecture.

4.1 Basic Idea

The objective of this study is to leverage an ML model to identify an effective power scaling factor combination that maximizes the covert rate while maintaining low computational complexity. In conventional grid search–based approaches, reducing the step size γ enables the exploration of effective power scaling factor combinations that are closer to the continuous solution. However, as γ decreases, the computational complexity increases significantly, potentially affecting for real-time implementation.

To overcome this limitation, this study employs an ML model to select an effective power scaling factor combination using effective channel gains and covertness-related features as inputs. In the proposed scheme, training is performed in the offline phase using several channel realizations, while in the online phase, the trained model can directly select an effective power scaling factor combination without resorting to an exhaustive search. Consequently, the proposed scheme significantly reduces computational complexity while achieving a performance close to that of the discretized grid-search baseline, making it suitable for practical covert communication systems.

4.2 DNN Architecture

The architecture of the proposed ML model is shown in Fig. 2. In this study, we consider a classification-based DNN. The proposed DNN employs channel gains and a covertness-related feature as inputs and learns to select an effective power scaling factor combination from a predefined set of candidate combinations. Considering instantaneous effective channel gains and a covertness feature, the trained DNN directly predicts an effective power scaling factor combination that satisfies the covertness constraint with low computational complexity.

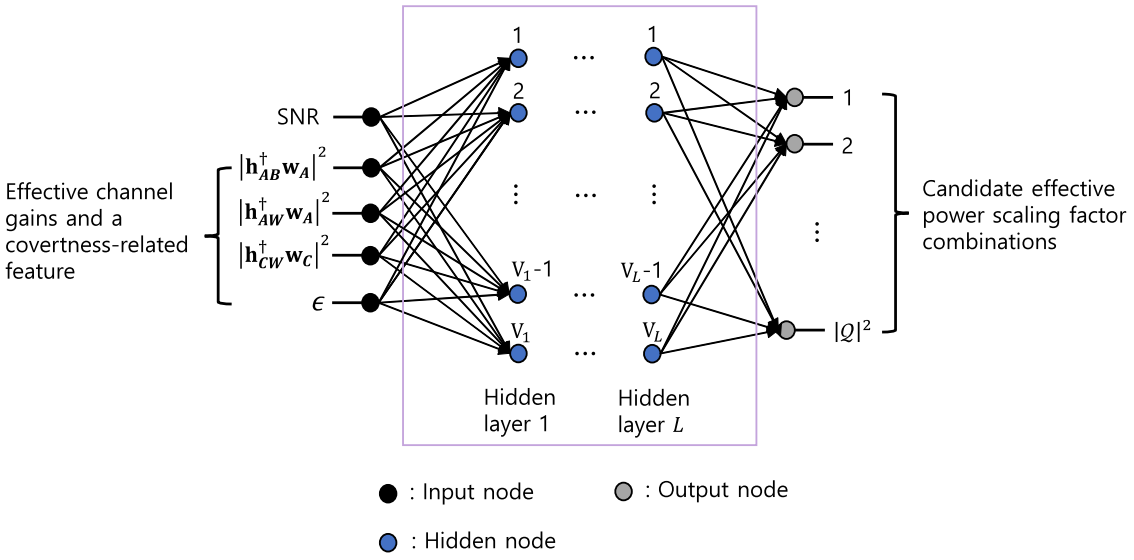

Figure 2: Architecture of the proposed ML-based power allocation model.

In LEO satellite communication environments, the channel conditions vary rapidly owing to the high mobility of LEO satellites. Therefore, it is crucial to select an effective power scaling factor combination that satisfies the covertness constraint with low computational complexity. As a result, instead of repeatedly solving complex continuous optimization problems, the proposed classification-based DNN provides an effective and practical solution for covert communication in LEO satellite systems. The input nodes consist of the signal-to-noise ratio (SNR), effective channel gain from Alice to Bob $|\mathbf{h}_{AB}^{\dagger}\mathbf{w}_A|^2$, effective channel gain from Alice to Willie $|\mathbf{h}_{AW}^{\dagger}\mathbf{w}_A|^2$, effective channel gain from Charlie to Willie $|\mathbf{h}_{CW}^{\dagger}\mathbf{w}_C|^2$, and the allowable detection error threshold ϵ. Since $n_B, n_W \sim \mathcal{CN}(0,1)$, the noise variance is normalized to unity. Therefore, the SNR in linear scale is equivalent to the transmit power, i.e., SNR = P_A = P_C. These input features are selected to include the instantaneous channel conditions and covertness requirements that directly affect the covert rate and detection performance, where the effective channel gains inherently incorporate channel fading, Doppler-induced phase variations, and array responses. The output layer consists of $|\mathcal{Q}|^2 = ((1/\gamma) + 1)^2$ nodes, each of which corresponds to an effective power scaling factor combination.

In addition, the proposed DNN comprises L hidden layers, where the lth hidden layer contains V_l hidden nodes. As activation functions, the rectified linear unit (ReLU) is applied in the hidden layers, and the softmax function is used in the output layer. The categorical cross-entropy function is adopted as the loss function, which is defined as:

$$\zeta = -\sum_{i=1}^{|\mathcal{Q}|^2} \varphi_i \log(c_i), \tag{33}$$

where φ_i and c_i denote the one-hot encoded label and predicted probability obtained from the softmax function, respectively. Moreover, early stopping is applied to prevent overfitting. The adaptive moment estimation (Adam) algorithm was employed for the optimization.

5 Numerical Results

In this section, we evaluate the performance of the proposed ML-based scheme for power allocation and compare it with that of the discretized grid-search baseline. The simulation parameters are summarized in Table 2. We consider a simulation environment where Alice is equipped with a (4×4)-element UPA antenna (i.e., $N_x = N_y = 4$) and the Rician K-factors of the Alice–Bob, Alice–Willie, Charlie–Bob, and Charlie–Willie channels are evaluated at 0, 10, and 20 (that is, $K_{AB} = K_{AW} = K_{CB} = K_{CW} \in \{0, 10, 20\}$). It is assumed that a block of 500 ($B = 500$) channels is used, and the allowable detection error probability is set to 0.05 ($\epsilon = 0.05$), which is fixed and consistently applied during both training and testing. The azimuth and elevation angles are denoted by $\phi \in [0, 2\pi)$ and $\theta \in [0, \pi/2]$, respectively. In addition, the inter-element spacing is set to $d = 1/2$ (i.e., $\lambda = 1$). The ML model included three hidden layers ($L = 3$), where the first, second, and third layers consisted of 300, 500, and 500 hidden nodes, respectively; that is, $(V_1, V_2, V_3) = (300, 500, 500)$.

Table 2: Simulation parameters.

Parameter	Value
UPA size at Alice	4×4 (i.e., $N_x = N_y = 4$)
Rician K-factors	$K_{AB} = K_{AW} = K_{CB} = K_{CW} \in \{0, 10, 20\}$
The number of observation samples	$B = 500$
Detection error probability	$\epsilon = 0.05$ (fixed for training/testing)
Azimuth angle range	$\phi \in [0, 2\pi)$
Elevation angle range	$\theta \in [0, \pi/2]$
Inter-element spacing	$d = 1/2$ (i.e., $\lambda = 1$)
Hidden layers	$L = 3$
Hidden nodes	$(V_1, V_2, V_3) = (300, 500, 500)$
Training samples	7×10^5 (80% train/20% validation)
Test samples	7×10^4
Optimizer	Adam
Learning rate	0.001
Batch size	210
Max epochs	1000
Early stopping	monitor val. loss, patience = 20 epochs

For training, 7×10^5-independent samples were generated, of which 80% were used for training and the remaining 20% were used for validation. The DNN was trained using the Adam optimizer with a learning rate of 0.001, a batch size of 210, and a maximum of 1000 epochs. To prevent overfitting, an early stopping was applied by monitoring the validation loss, and the training was terminated if no improvement in the validation loss was observed for 20 consecutive epochs. The trained model was evaluated using 7×10^4-independent test samples. During the generation of training and test data, for each channel realization, all discretized candidate effective power scaling factor combinations were considered, and the combination that maximizes the covert rate computed according to (32) was selected as the target label. In the testing

phase, after the DNN outputs an effective power scaling factor combination for a given channel realization, the covert rate of the DNN output is computed according to (32) and used to evaluate the performance of the DNN. Simulations were conducted using MATLAB and the TensorFlow framework. Specifically, MATLAB was used to generate training and test samples, whereas TensorFlow was employed to implement the DNN architecture.

Figs. 3–5 compare the average covert rate of the proposed scheme with that of the discretized grid-search baseline, where the step size of the effective power scaling factor is set to 0.1 ($\gamma = 0.1$). Under this configuration, the proposed model consists of five fixed input nodes and 121 ($|\mathcal{Q}|^2 = 121$) output nodes. For each K-factor, the same DNN architecture is adopted, while the model is trained independently using the corresponding dataset. Here, the *Discretized grid-search baselines (with UAV jammer, $\gamma = 0.1$ and $\gamma = 0.001$)* refer to the cases where Charlie is present, whereas the *Discretized grid-search baseline (no UAV jammer)* corresponds to the scenario where only Alice is present. As shown in Figs. 3–5, the proposed scheme achieves a comparable average covert rate to that of the discretized grid-search baseline with $\gamma = 0.1$. For each case, the proposed scheme achieves classification accuracies of 97.59%, 90.09%, and 93.87% in Figs. 3–5, respectively. In contrast, when a finer discretization with $\gamma = 0.001$ is employed, the discretized grid-search baseline exhibits a higher covert rate than that obtained with $\gamma = 0.1$, indicating that the covert constraint is highly sensitive to the effective power scaling factor discretization.

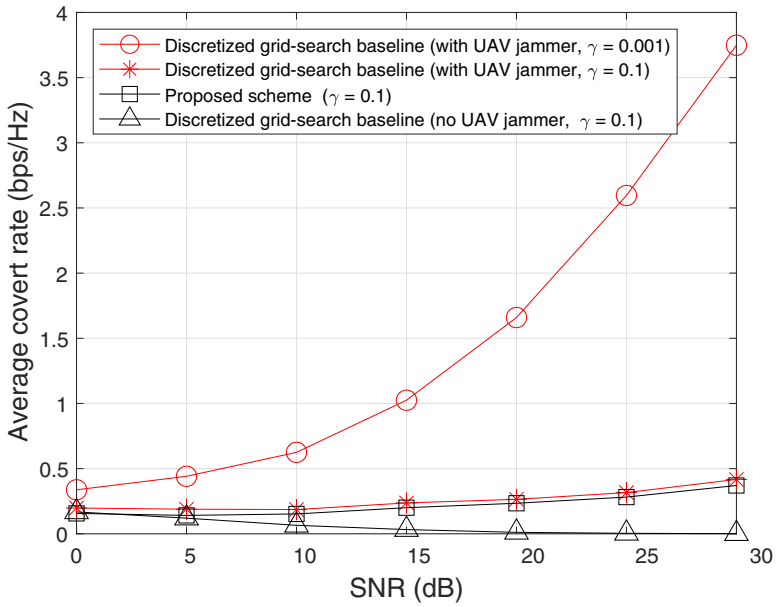

Figure 3: Average covert rate of different schemes under Rician fading with K-factor = 0 and $\gamma = 0.1$.

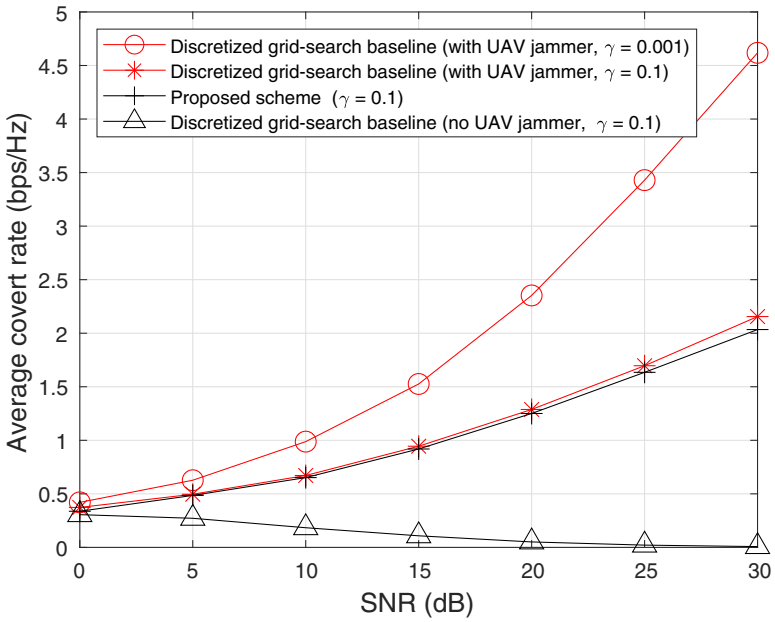

Figure 4: Average covert rate of different schemes under Rician fading with K-factor = 10 and γ = 0.1.

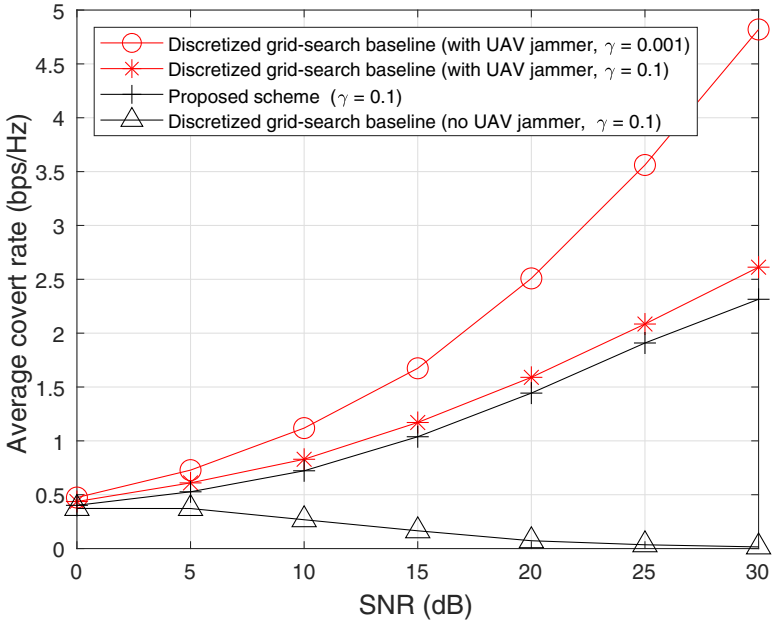

Figure 5: Average covert rate of different schemes under Rician fading with K-factor = 20 and γ = 0.1.

Fig. 6 compares the average covert rate performance of the proposed scheme with that of the discretized grid-search baseline using a step size of γ = 0.01 for the effective power scaling factors. As shown in the figure, the discretized grid-search baseline with γ = 0.01 achieves a lower covert rate than that obtained with γ = 0.001, while exhibiting performance relatively close to that of the baseline with γ = 0.1. In contrast, the proposed scheme shows overall lower covert rate performance than the discretized grid-search baseline with γ = 0.01, and the corresponding classification accuracy of the proposed scheme is approximately 47%.

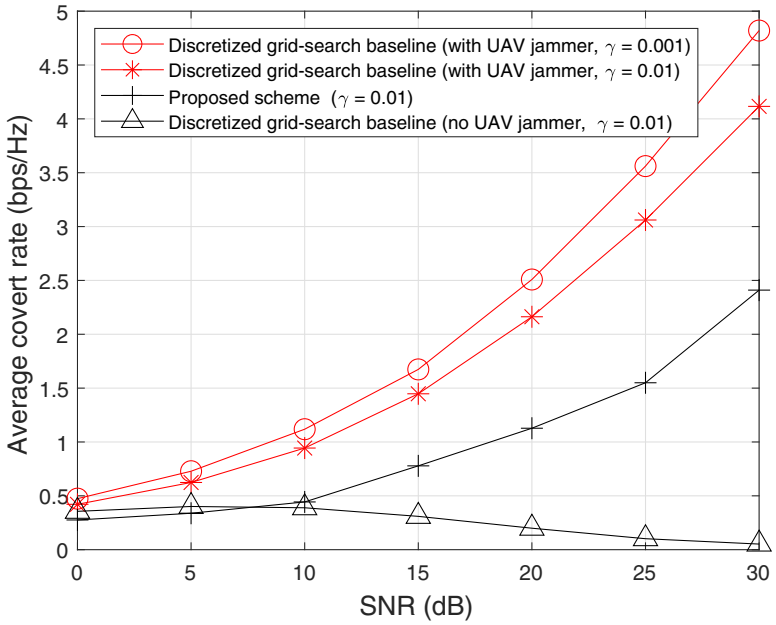

Figure 6: Average covert rate of different schemes under Rician fading with K-factor = 10 and γ = 0.01.

This performance gap can be attributed to the simultaneous increase in the classification difficulty and the size of the search space as the effective power scaling factor discretization becomes finer. When the step size of the effective power scaling factors is relatively large, i.e., γ = 0.1, the number of candidate effective power scaling factor combinations is limited to 121, rendering the classification problem relatively simple. Under this condition, the proposed scheme is able to achieve a comparable average covert rate to that of the discretized grid-search baseline. However, when the step size of the effective power scaling factors is reduced to γ = 0.01, the number of candidate values for each effective power scaling factor increases, leading to a rapid expansion of the search space to 10,201 combinations. As a result, the classification task becomes significantly more challenging, making it more difficult for the proposed scheme to accurately predict the effective power scaling factor combination. Consequently, a degradation in covert rate performance is observed compared to the discretized grid-search baseline with γ = 0.01. The measured classification accuracy of approximately 47% in this experiment supports this observation. In general, decreasing the step size of the effective power scaling factors enables the discretized grid-search baseline to approach the continuous optimal solution and achieve improved covert rate performance. However, the associated computational complexity increases rapidly, since the size of the search space grows quadratically as the step size γ used to discretize the effective power scaling factors decreases. This reveals an inherent trade-off between covert rate performance and computational complexity.

Nevertheless, the proposed scheme offers a notable computational advantage in terms of computational efficiency. To ensure a fair comparison, the runtime is evaluated only for the decision stage using pre-generated inputs, while preprocessing steps such as channel generation, beamforming, and effective channel gain computation are not included. This is because these operations are common to both the proposed scheme and the discretized grid-search baseline and are independent of the decision-making process. All runtime evaluations are conducted under the same batch size of 1024 on an Intel(R) Core(TM) i7-9700 CPU @ 3.00 GHz using TensorFlow 2.4.1, ensuring a fair comparison of the inference complexity. Both the proposed scheme and the discretized grid-search baseline are evaluated under the same runtime evaluation protocol. Therefore, the real-time practicality claim is limited to the inference stage under the validated

experimental configuration described above. Under this setting, the proposed scheme achieves an average inference time of approximately 0.069 ms per sample, whereas the discretized grid-search baseline with $\gamma = 0.01$ requires approximately 0.32 ms per sample. That is, in terms of average runtime, the proposed scheme achieves approximately 4 to 5 times less inference time than the discretized grid-search baseline. Although the classification accuracy of the proposed scheme degrades when a finer discretization of the effective power scaling factors with a smaller step size γ is used (e.g., $\gamma = 0.01$), sufficiently high accuracy is achieved under a coarser discretization setting (e.g., $\gamma = 0.1$). Leveraging this observation, the proposed scheme can be used as an efficient front-end mechanism to identify promising candidate regions or coarse effective power scaling factor combinations. These candidates can then be further examined using more fine-grained search procedures, if needed. In this sense, the proposed scheme serves as an efficient front-end mechanism that significantly reduces the computational burden while preserving competitive covert rate performance.

To further quantify this advantage, the computational complexity of the proposed scheme can be expressed as:

$$\mathcal{O}\left(5V_1 + \sum_{l=1}^{L-1} V_l V_{l+1} + V_L|\mathcal{Q}|^2\right). \tag{34}$$

For the discretized grid-search baseline, the computational complexity scales with the number of candidate effective power scaling factor combinations and can be expressed as:

$$\mathcal{O}\left(|\mathcal{Q}|^2\right). \tag{35}$$

Fig. 7 illustrates the impact of the allowable detection error probability on the average covert rate, where the detection error probability is varied with a step size of 0.01 and the SNR is fixed at 15 dB under Rician fading with K-factor = 10. As the allowable detection error probability ϵ increases, the covert constraint becomes less restrictive, allowing higher transmit power. Consequently, the achievable covert rate increases.

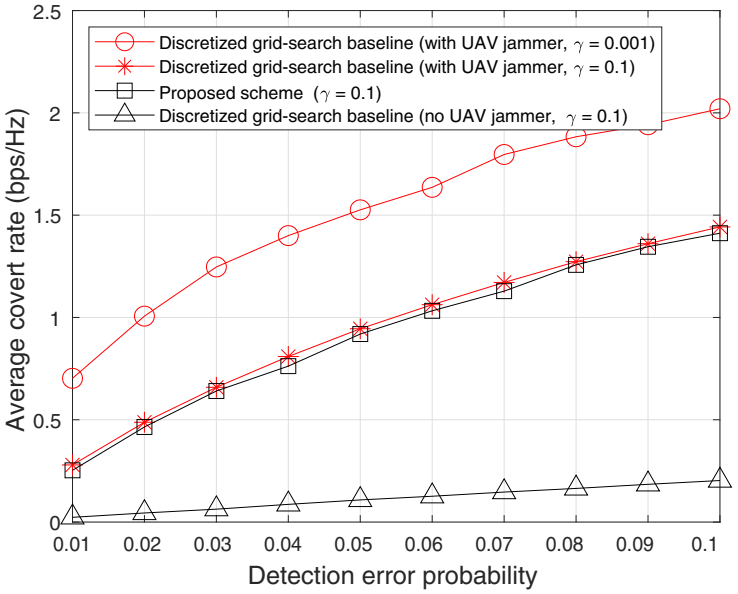

Figure 7: Average covert rate of the detection error probability, varied from 0.1 to 0.01 with a step size of 0.01, for SNR = 15 dB and Rician K-factor = 10.

To assess robustness against random initialization, experiments were conducted over five independent random seeds. Table 3 summarizes the mean and standard deviation (SD) of the average covert rate across SNR values, while Table 4 reports the classification accuracy for each seed. The reported statistics show only minor variation across different seeds.

Table 3: Average covert rate over five independent random seeds (mean ± standard deviation (SD)).

SNR (dB)	Proposed Scheme (mean ± SD)	Discretized Grid-Search Baseline (mean ± SD)
0	0.3395 ± 0.0181	0.3680 ± 0.0045
5	0.4773 ± 0.0081	0.4951 ± 0.0048
10	0.6599 ± 0.0089	0.6773 ± 0.0086
15	0.9395 ± 0.0162	0.9663 ± 0.0139
20	1.2767 ± 0.0251	1.3163 ± 0.0206
25	1.6478 ± 0.0108	1.7001 ± 0.0157
30	2.0643 ± 0.0195	2.1527 ± 0.0274

Table 4: Classification accuracy over five independent random seeds.

Seed	Accuracy (%)
1	90.09
2	92.48
3	92.65
4	89.26
5	92.30

6 Conclusion

In this study, we proposed an ML–based power allocation scheme for covert communication in LEO satellite–UAV cooperative networks. By utilizing the cooperation between the LEO satellite and the UAV, the proposed scheme effectively enhances the covert transmission performance while significantly reducing the computational complexity associated with power allocation. Numerical results demonstrate that, with a moderate step size of the effective power scaling factors, the proposed scheme achieves a comparable average covert rate to that of the discretized grid-search baseline, while significantly reducing the computational complexity. As the step size decreases, the performance gap between the proposed scheme and the discretized grid-search baseline becomes more pronounced, revealing an inherent scalability trade-off in learning-based approaches as the action space expands. Despite this trade-off, the proposed scheme provides a notable computational advantage under the considered operating regimes, achieving several-fold speedup over exhaustive grid search. This study is conducted based on a simplified LEO satellite–UAV cooperative network environment. Future work will extend the proposed framework to more practical scenarios by considering multiple wardens and multiple UAVs, the energy consumption of UAVs, the effects of channel estimation errors and delays, and learning frameworks that explicitly exploit temporal correlation in time-varying LEO channels with Doppler effects, as well as scalable learning architectures to address the scalability and accuracy challenges arising from large action spaces.

Acknowledgement: This manuscript is a supplementary and extended version of the paper presented at the 9th International Symposium on Mobile Internet Security (MobiSec'25) Conference. Building upon the conference version,

it adopts a more realistic channel model, improves the resolution of the power allocation search, and further extends the analysis and numerical evaluation of the detection performance and covert communication constraints, thereby significantly enhancing the analytical and experimental completeness of the study.

Funding Statement: This work was supported by the MSIT under the ICAN (ICT Challenge and Advanced Network of HRD) Program (No. IITP-2022-RS-2022-00156310) supervised by the Institute of Information & Communication Technology Planning & Evaluation (IITP). The work of Jung Hoon Lee was supported in part by Hankuk University of Foreign Studies Research Fund.

Author Contributions: The authors confirm contribution to the paper as follows: Conceptualization, Minjeong Kang and Jung Hoon Lee; methodology, Minjeong Kang; software, Minjeong Kang; validation, Minjeong Kang, Jung Hoon Lee and Il-Gu Lee; formal analysis, Minjeong Kang; investigation, Minjeong Kang; resources, Il-Gu Lee; data curation, Minjeong Kang; writing—original draft preparation, Minjeong Kang; writing—review and editing, Jung Hoon Lee and Il-Gu Lee; visualization, Minjeong Kang; supervision, Jung Hoon Lee and Il-Gu Lee; project administration, Il-Gu Lee; funding acquisition, Il-Gu Lee. All authors reviewed and approved the final version of the manuscript.

Availability of Data and Materials: The data that support the findings of this study are available from the corresponding author upon reasonable request.

Ethics Approval: Not applicable.

Conflicts of Interest: The authors declare no conflicts of interest.

Abbreviations

LEO	Low Earth Orbit
UAV	Unmanned Aerial Vehicle
UPA	Uniform Planar Array
ULA	Uniform Linear Array
LoS	Line-of-Sight
NLoS	Non-Line-of-Sight
AN	Artificial Noise
MRT	Maximum Ratio Transmission
ZF	Zero-Forcing
SNR	Signal-to-Noise Ratio
SINR	Signal-to-Interference-Plus-Noise Ratio
ML	Machine Learning
DNN	Deep Neural Network
PLS	Physical-Layer Security
IRS	Intelligent Reflecting Surface
RIS	Reconfigurable Intelligent Surface
CSI	Channel State Information
MIMO	Multiple-Input Multiple-Output
MISO	Multiple-Input Single-Output
SD	Standard Deviation

References

1. Chen X, An J, Xiong Z, Xing C, Zhao N, Yu FR, et al. Covert communications: a comprehensive survey. IEEE Commun Surveys Tuts. 2023;25(2):1173–98.
2. Shahzad K, Zhou X. Covert wireless communications under quasi-static fading with channel uncertainty. IEEE Trans Inf Forensics Secur. 2021;16:1104–16. doi:10.1109/TIFS.2020.3029902.

3. Ryu JY, Lee JH. Covert communications via full-duplex user relaying. Sensors. 2025;25(12):3614. doi:10.3390/s25123614.
4. Gao C, Yang B, Zheng D, Jiang X, Taleb T. Cooperative jamming and relay selection for covert communications in wireless relay systems. IEEE Trans Commun. 2024;72(2):1020–32. doi:10.1109/twc.2009.090323.
5. Forouzesh M, Azmi P, Kuhestani A, Yeoh PL. Covert communication and secure transmission over untrusted relaying networks in the presence of multiple wardens. IEEE Trans Commun. 2020;68(6):3737–49. doi:10.1109/TCOMM.2020.2978206.
6. Jin Q, Fan L, Lei X, Zhao J, Nallanathan A. Covert communication of multi-antenna AF relaying networks. IEEE Trans Commun. 2025;73(8):5699–714. doi:10.1109/TCOMM.2025.3534475.
7. Wang C, Chen X, An J, Xiong Z, Xing C, Zhao N, et al. Covert communication assisted by UAV-IRS. IEEE Trans Commun. 2023;71(1):357–69. doi:10.1109/tcomm.2022.3220903.
8. Li X, Liu M, Dang S, Luong NC, Yuen C, Nallanathan A, et al. Covert communications with enhanced physical layer security in RIS-assisted cooperative networks. IEEE Trans Wirel Commun. 2025;24(7):5605–19. doi:10.1109/TWC.2025.3548024.
9. Jiang X, Chen X, Tang J, Zhao N, Zhang XY, Niyato D, et al. Covert communication in UAV-assisted air-ground networks. IEEE Wirel Commun. 2021;28(4):190–7. doi:10.1109/mwc.001.2000454.
10. Wang Y, Guo K, Wu Z, Wu M, Nauman A, Cheng J, et al. Covert communication for satellite aerial-ground integrated networks under imperfect limitations. IEEE Internet Things J. 2026;13(1):296–307. doi:10.1109/JIOT.2025.3601506.
11. Mu S, Lei H, Park KH, Pan G. Finite block-length covert communication in space-air–ground integrated networks. IEEE Internet Things J. 2026;13(1):1–12. doi:10.1109/JIOT.2025.3531881.
12. Feng S, Lu X, Sun S, Hossain E, Wei G, Ni Z. Covert communication in large-scale multi-tier LEO satellite networks. IEEE Trans Mob Comput. 2024;23(12):11576–87. doi:10.1109/tmc.2024.3396793.
13. Zhang R, Chen X, Liu M, Zhao N, Wang X, Nallanathan A. UAV relay assisted cooperative jamming for covert communications over Rician fading. IEEE Trans Veh Technol. 2022;71(7):7936–41. doi:10.1109/tvt.2022.3164051.
14. He Y, Huang F, Wang D, Zhou X, Zhang R. Uplink outage probability analysis of AAV and intelligent connected vehicle cooperative communication using full-duplex MIMO. IEEE Commun Lett. 2025;29(9):2068–72. doi:10.1109/LCOMM.2025.3585337.
15. Wang J, Gong S, Xiao J, Guo P, Wang J, Xie W, et al. A lightweight channel prediction network for UAV-LEO satellite communications. IEEE Wirel Commun Lett. 2025;14(1):113–7. doi:10.1109/lwc.2024.3489677.
16. Kang MJ, Lee JH, Ryu JY. Machine learning-based NOMA for multiuser MISO broadcast channels. IEEE Commun Lett. 2024;28(1):93–7. doi:10.1109/lcomm.2023.3338475.
17. Zhou D, Sheng M, Wang Y, Li J, Han Z. Machine learning-based resource allocation in satellite networks supporting Internet of Remote Things. IEEE Trans Wirel Commun. 2021;20(10):6606–21. doi:10.1109/twc.2021.3075289.
18. Minani F, Kobayashi M, Fujihashi T, Alim MA, Saruwatari S, Nishi M, et al. Channel prediction and fair resource allocation for NTN uplinks by LSTM and deep reinforcement learning. IEEE Trans Wirel Commun. 2025;24(10):8311–30. doi:10.1109/TWC.2025.3565774.
19. Kim D, Jung H, Lee IH. DQN-based scheduling algorithm for beam-hopping LEO satellite communication systems. IEEE Wirel Commun Lett. 2025;14(8):2401–5. doi:10.1109/LWC.2025.3570783.
20. Lee C, Bang I, Kim T, Lee H, Jung BC, Chae SH. Multi-agent deep reinforcement learning based handover strategy for LEO satellite networks. IEEE Commun Lett. 2025;29(5):1117–21. doi:10.1109/LCOMM.2025.3554818.
21. Sui X, Jiang Z, Lyu Y, Fan R, Hu H, Liu Z. Integrating convex optimization and deep learning for downlink resource allocation in LEO satellite networks. IEEE Trans Cogn Commun Netw. 2024;10(3):1104–18. doi:10.1109/tccn.2024.3361071.
22. Sun M, Zhang Q, Yao H, Gao R, Zhao Y, Guizani M. Resource allocation and deep learning-based joint detection scheme in satellite NOMA systems. IEEE Trans Wirel Commun. 2025;24(1):526–39. doi:10.1109/twc.2024.3496089.
23. Li J, Wang D, Zhao H, Jin Y, He Y, Zhou F, et al. Enhancing secrecy energy efficiency in UAV-RIS assisted mobile IoV networks through DRL. IEEE Trans Wirel Commun. 2026;25:2092–108. doi:10.1109/TWC.2025.3594691.